Biosensors and Bioelectronics 132 (2019) 286–293

Contents lists available at ScienceDirect

Biosensors and Bioelectronics

journal homepage: www.elsevier.com/locate/bios

Luminescent CeO_2:Eu^{3+} nanocrystals for robust *in situ* H_2O_2 real-time detection in bacterial cell cultures

Dorian F. Henning[a,1], Padryk Merkl[a], Changhun Yun[a], Federico Iovino[a,b], Ling Xie[c], Eleftherios Mouzourakis[d], Constantinos Moularas[d], Yiannis Deligiannakis[d], Birgitta Henriques-Normark[a,b], Klaus Leifer[c], Georgios A. Sotiriou[a,*]

[a] Department of Microbiology, Tumor and Cell Biology, Karolinska Institutet, SE-1 71 77 Stockholm, Sweden
[b] Department of Clinical Microbiology, Karolinska University Hospital, SE-171 76 Stockholm, Sweden
[c] Applied Materials Science, Department of Engineering Sciences, Ångström Lab, Uppsala University, SE-752 37 Uppsala, Sweden
[d] Department of Physics, University of Ioannina, Panepistimioupoli, GR-451 10 Ioannina, Greece

ARTICLE INFO

Keywords:
Nanozymes
Rare-earth doped nanoparticles
Hydrogen peroxide
Flame nanoparticle synthesis

ABSTRACT

Hydrogen peroxide (H_2O_2) quantification in biomedicine is valuable as inflammation biomarker but also in assays employing enzymes that generate or consume H_2O_2 linked to a specific biomarker. Optical H_2O_2 detection is typically performed through peroxidase-coupled reactions utilizing organic dyes that suffer, however, from poor stability/reproducibility and also cannot be employed *in situ* in dynamic complex cell cultures to monitor H_2O_2 levels in real-time. Here, we utilize enzyme-mimetic CeO_2 nanocrystals that are sensitive to H_2O_2 and study the effect of H_2O_2 presence on their electronic and luminescent properties. We produce and dope with Eu^{3+} these particles in a single-step by flame synthesis and directly deposit them on Si and glass substrates to fabricate nanoparticle layers to monitor in real-time and *in situ* the H_2O_2 concentrations generated by *Streptococcus pneumoniae* clinical isolates. Furthermore, the small CeO_2:Eu^{3+} nanocrystals are combined in a single-step with larger, non-responsive Y_2O_3:Tb^{3+} nanoparticles during their double-nozzle flame synthesis to engineer hybrid luminescent nanoaggregates as ratiometric robust biosensors. We demonstrate the functionality of these biosensors by monitoring their response in the presence of a broad range of H_2O_2 concentrations *in vitro* from *S. pneumoniae*, highlighting their potential for facile real-time H_2O_2 detection *in vitro* in cell cultures.

1. Introduction

Inorganic materials with enzyme-mimetic properties, the so-called nanozymes, are an emerging type of materials with decisive applications in healthcare (Wei and Wang, 2013). Among them perhaps the most well-known are CeO_2 nanoparticles (Walkey et al., 2015; Gupta et al., 2016) that exhibit both catalase and superoxide dismutase mimetic properties depending on the oxidation state of the Ce atoms on their surface (Lee et al., 2013; Li et al., 2015; Wang et al., 2015). Such CeO_2 crystalline nanoparticles (nanocrystals) readily interact with hydrogen peroxide (H_2O_2) in solution due to their redox potential (Lee et al., 2013; Wang et al., 2015). This type of interaction has led towards the development of H_2O_2 sensors, for example by their optical absorption (Lee et al., 2013), but also recently by doping these nanocrystals with a rare-earth ion (Eu^{3+}) that renders them luminescent and by monitoring their luminescence quenching (Pratsinis et al., 2017). The small size of such CeO_2: Eu^{3+} nanocrystals enables them as highly-sensitive H_2O_2 biosensors with limit-of-detection (LOD) down to the nM levels (Pratsinis et al., 2017).

H_2O_2 plays a major role in biomedicine; for example high H_2O_2 concentrations are released as host defense mechanism during infection or infammation *in vivo* (Halliwell et al., 2000) while its presence is correlated with several diseases (Yang et al., 2015, 2016). Furthermore, H_2O_2 quantification is important for *in vitro* enzyme-linked assays (*e.g.* ELISA) that generate or consume H_2O_2 rendering it also a potential intermediary biomolecule for detection of other disease-specific biomarkers (de la Rica and Stevens, 2012). Low LODs are attractive, however, robustness and stability of biosensors becomes increasingly more important due to the complexity of biological systems that typically contain biomolecules, organisms and metabolic byproducts (Duee et al., 2015; Liu et al., 2015). Even though several electrochemical methods to detect H_2O_2 at low concentrations have been reported

* Corresponding author.
E-mail address: georgios.sotiriou@ki.se (G.A. Sotiriou).
[1] Current address: Department of Computing, Imperial College London, UK.

https://doi.org/10.1016/j.bios.2019.03.012
Received 7 December 2018; Received in revised form 6 March 2019; Accepted 8 March 2019
Available online 08 March 2019
0956-5663/

(Gupta et al., 2017), commercially-available assays for the optical detection typically utilize enzyme-based dyes (colori-/fluorimetric detection) through peroxidase-coupled reactions. These assays suffer from low optical and chemical stability, precision and detection speed and cannot be employed to monitor in real-time H_2O_2 concentrations *in situ* during *in vitro* biological experiments with cells (Duee et al., 2015). These drawbacks have prompted several groups to develop alternative materials for H_2O_2 sensing such as lanthanide coordination polymer-based ones (Zeng et al., 2016, 2017) but also sensors from inorganic materials, and thus more stable than organic dyes, luminescent nanomaterials that are sensitive to H_2O_2 for its optical detection, such as CeO_2:Eu^{3+} nanocrystals (Yuan et al., 2009; Lv et al., 2014; Zheng et al., 2014; Duee et al., 2015; Pratsinis et al., 2017).

Here, we rationally design and produce small (~5 nm) CeO_2:Eu^{3+} nanocrystals by flame spray pyrolysis, a nanomanufacturing process famous for its scalability and reproducibility (Pratsinis, 2010). We perform detailed morphological characterization and further study their interaction with H_2O_2 with electron paramagnetic resonance spectroscopy to identify the electronic changes in the CeO_2:Eu^{3+} nanocrystals. Furthermore, we fabricate functional nanoparticle films on Si and glass substrates by flame aerosol deposition and *in situ* flame annealing (Tricoli et al., 2008) of the freshly-formed CeO_2:Eu^{3+} nanocrystals and monitor in real-time the effect of H_2O_2 on their luminescence in bacterial cell cultures *in situ* with *Streptococcus pneumoniae* (the pneumococcus) clinical isolates. *S. pneumoniae* is a main cause of pneumonia, sepsis and meningitis and one of the most common cause of death worldwide (Henriques-Normark and Tuomanen, 2013; Iovino et al., 2016). Some clinically-relevant *S. pneumoniae* strains generate high levels of H_2O_2 as part of their aerobic metabolism. The produced H_2O_2 can inhibit the growth of other nasopharyngeal flora members such as *Haemophilus influenzae* and *Neisseria meningitidis* and can have cytotoxic effect both *in vivo* and *in vitro* on human epithelial and endothelial cells (Andisi et al., 2012). Pneumococci convert pyruvate to acetyl phosphate and H_2O_2 *via* a pyruvate oxidase enzyme encoded by the spxB gene (Spellerberg et al., 1996; Syk et al., 2014).

Finally, we further explore the suitability of flame nanoparticle synthesis towards the development of a ratiometric H_2O_2 biosensor based on a single-step double-nozzle flame spray pyrolysis (Strobel et al., 2006) of multicomponent nanoparticles. Double-nozzle flame synthesis is one of the latest developments of this nanomanufacture process (Pratsinis, 2010) that allows for the production of multicomponent nanoparticle systems with independent control of the product particle size and morphology from each nozzle (Grossmann et al., 2015). This technology has been used so far only for production of nanoparticles tailored for catalysis (Büchel et al., 2009). Here, we extend this process for the fabrication of bioresponsive materials and we explore the synthesis of enzyme-mimetic luminescent and H_2O_2-responsive CeO_2:Eu^{3+} nanoparticles that are mixed in the nanoscale within the same agglomerates/aggregates with larger luminescent non-responsive (~30 nm) Y_2O_3:Tb^{3+} nanoparticles. Both components from this nanoparticle system are excited at the same near-UV wavelength and their emission wavelengths are monitored as a function of H_2O_2 concentrations. The robustness of these biosensors is further explored under realistic conditions by detecting H_2O_2 concentrations *in vitro* from *S. pneumoniae* cultures.

2. Materials and methods

2.1. Particle synthesis and characterization

CeO_2 and Y_2O_3 nanoparticles were produced by flame spray pyrolysis (FSP), by dispersing a liquid precursor solution containing 0.3 M cerium 2-ethylhexanoate (49% in 2-ethylhexanoic acid, Alfa Aesar) and 5 at% europium nitrate hexahydrate (99.9%, Alfa Aesar), or 0.4 M yttrium nitrate hexahydrate (99.8%, Aldrich) and 2.5 at% terbium nitrate hydrate (99.9%, Alfa Aesar) dissolved in a 1:1 ratio of 2-ethylhexanoic acid (99%, Alfa Aesar) and ethanol (99.96%, Alfa Aesar). The dual nozzle nanoparticles were synthesized using the previously described precursors and the same process with an alternative set-up, described by Strobel et al. with a flame angle of 60 degrees. The solution was fed through a capillary from 100 mL syringes (SGE Analytical Science) by syringe pumps (New Era Pump Systems, Inc.) at rates of 3 or 5 mL/min and 12 mL/min, respectively. The precursor was subsequently dispersed by an oxygen (> 99.5%, AGA Gas AB) flow at a rate of 8 or 5 L/min and 3 L/min (EL-FLOW Select, Bronkhorst), respectively. The spray was ignited by a premixed support flame of methane/oxygen (> 99.5%, AGA Gas AB) at flow rates of 1.5 L/min and 3.2 L/min respectively. The particles were collected on a glass fiber filter (Albet LabScience) with the aid of a Mink MM 1144 BV vacuum pump (Busch). Nanoparticle films were deposited on Si and glass substrates by mounting them on a water-cooled substrate holder and placing them 18 cm above the nozzle for 60 s. The films were subsequently flame annealed by an impinging particle-free (ethanol) flame by placing the substrates 15 cm above the nozzle for 15 s. The Si-substrates were mounted on a custom-made 3D printed (Wanhao Duplicator 4S) flow cell (ABS) and placed inside the spectrophotometer. For deposition on glass substrates, deposition time was 45 s at 18 cm above the nozzle and annealed for 10 s at 15 cm above the nozzle.

The powder X-ray diffraction of the particles was performed with a Rigaku MiniFlex (1.5406 Å Cu Kα1 radiation; step size 0.01°). Rietveld refinement was performed using the Rigaku software. The specific surface area (SSA) was determined using nitrogen absorption performed on a Gemini VII 2390 (Micromeritics) after degassing at 150 °C for at least 3 h. Scanning electron microscopy was performed on a Zeiss Ultra 55 equiped with field emission gun (FESEM). Scanning transmission electron microscopy (STEM) and EDX analysis was performed with an aberration-corrected TEM (Titan Themis) operated with an acceleration voltage of 200 kV. The chemical analysis is performed by STEM-EDX and the beam current was set to 24 nA for an acquisition time of 30 min. Quantification was performed on the Esprit (Bruker), after background subtraction and deconvolution on different X-ray lines. For the TEM, nanoparticles were suspended in ethanol by bath ultrasonication and one drop of the suspension was deposited onto a 3 mm carbon coated copper grid. The thickness of the carbon film is about 10 nm. The TEM grid was dried in the air for 14 h. Before the TEM measurements, 2 min plasma cleaning was applied on the samples in order to remove hydrocarbon contamination. The size of nanoparticles is measured by manually drawing an intensity profile across one nanoparticle and 90% threshold value is chosen to measure the diameter of nanoparticles. The measurement error is in a range of ± 0.14 nm. EPR spectra were recorded with a Bruker ER200D spectrometer at liquid N_2 temperature 77 K. EPR spectra were recored for 10 mg of nanoparticles in quarz tubes (Suprasil, 5 mm, Wilmad Glass). The estimated concentration of the variosu Ce^{3+} centers per mass of material, the EPR signal intensity of each species was quantified based on numerical simulation and double integration of the signal and spin calibration using DPPH. EPR conditions: modulaiton amplitude 6 Gpp, modulation fequency 100 kHz. The evolution of the Ce^{3+} and Eu^{2+} centers before and addition of H_2O_2 were monitored *in situ* by freeze quenching the sample at 77 K after a predefined incubation time. X-ray photoelectron spectroscopy (XPS) spectra were recorded using SPECS spectrometer equipped with a twin Al-Mg anode X-ray source and a multichannel hemispherical sector electron analyzer (HSA-Phoibos 100). A monochromatized Mg Kα line at 1253.6 eV and analyzer pass energy of 20 eV were used in all XPS measurements. The binding energies were calculated with reference to the energy of C1s carbon peak at 284.5 eV. The surface composition of all samples in terms of atomic ratios was calculated, using a Shirley background and empirical cross section factors for XPS. Dynamic light scattering was performed with a Malvern Zetasizer upon the nanoparticle dispersion in aqueous solutions by ultrasonication.

2.2. Phosphorescence characterization and H_2O_2 sensing

Emission and excitation spectra, as well as sensor response measurements were performed using a LS 55 spectrophotometer (Perkin Elmer) with the well plate reader accessory and black, flat bottom, 96-well plates (Perkin Elmer). All measurements were performed in solution, either MilliQ DI water (Advantage A10, Millipore), or C+Y bacteria medium with varying nanoparticle and H_2O_2 concentrations. Different concentrations of H_2O_2 were titrated from a standard solution (Alfa Aesar, 35% w/w aq. sol.) and stored for maximum 24 h at 4 °C. Slit width was held constant throughout the measurements at 15 nm for excitation and 20 nm for emission. The single read measurements were averaged over 1 s for each measured wavelength. The photomultiplier voltage was set to 900 V for all measurements and neither excitation nor emission filter were used. Excitation light bulb settings were held constant throughout the measurements with gate time of 5 ms and delay of 0.1 ms. Ratiometric sensor response S_R was calculated by $S_R = 1-(R_S/R_0)$, where R_S is the ratiometric (I_{590}/I_{545}) signal of samples with various H_2O_2 concentrations, and R_0 is the ratiometric signal of pure H_2O.

2.3. H_2O_2 production by S. pneumoniae clinical isolates and in vitro biosensing

All pneumococcal strains were cultured on blood agar plates for 24 h and in semisynthetic C+Y medium and incubated overnight at 37 °C and 5% CO_2. The strains were grown until mid-log phase (OD_{620} 0.3–0.4) in liquid culture. For H_2O_2 measurements, the strains were lysed using penicillin (Sigma Aldrich) and stored at 4 °C. Nanoparticles in C+Y solution (2 g/L) were added to the bacterial cultures to a final concentration of 1 g/L. After 30 min of incubation time at 4 °C and vortex mixing every 5 min, the solutions were measured under the same conditions as the H_2O_2 calibration curve. Calculation of the H_2O_2 concentration was performed by logarithmic interpolation between two measurement points from the calibration curve.

2.4. High-resolution fluorescence microscopy

Nanoparticle films were deposited on Si and glass substrates that were placed at the bottom of multi-well plates. Imaging was performed with DV Elite microscope (Applied Precision) using a scientific complementary metal-oxide-semiconductor (sCMOS) camera. Images were acquired using Softworx (Applied Precision). Luminescence quenching was analyzed performing continuous imaging for 90 min (one snapshot every 15 s), using 100X magnification objective, excitation at 350 nm wavelength and emission at 594 nm wavelength.

3. Results and discussion

3.1. Particle morphology and interaction with hydrogen peroxide

Enzyme-mimetic CeO_2 nanocrystals are made by flame spray pyrolysis and doped in a single step with Eu^{3+} ions (5 at%) (Pratsinis et al., 2017). The crystal structure of the as-prepared nanoparticles is evaluated by X-ray powder diffraction (XRD) as shown in Fig. 1a, in which the characteristic cubic CeO_2 (solid circles, ICSD: 61595) crystal phases are present. There are no separate XRD peaks corresponding to any Eu-oxide crystal phases, indicating the incorporation of Eu^{3+} in the CeO_2 crystal lattice. The average crystallite size of the CeO_2:Eu^{3+} nanoparticles is calculated by Rietveld refinement analysis and corresponds to d_{XRD} = 4.1 nm, in agreement to the literature for such nanoparticles made by identical process conditions (Pratsinis et al., 2017). The specific surface area of the CeO_2:Eu^{3+} nanoparticles as determined by N_2 adsorption is 185 m^2/g that would correspond to an average primary particle diameter (Sauter mean diameter) d_{BET} = 4.4 nm, assuming monodispersed solid spherical particles with homogeneous density.

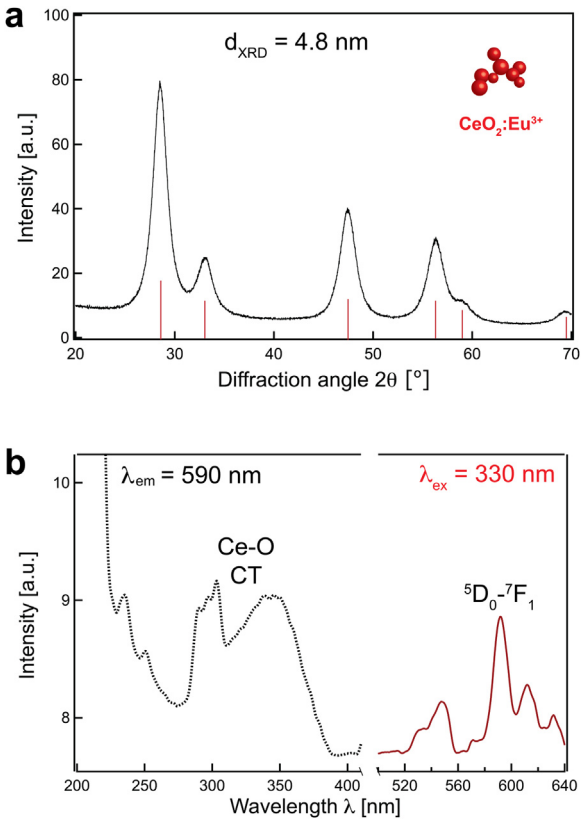

Fig. 1. (a) X-ray diffraction patterns of the CeO_2:Eu^{3+} nanocrystals, along with the diffraction peak positions for the cubic CeO_2 (standard ICSD card shown in red lines). The average crystallite size d_{XRD} is also shown as determined by Rietveld refinement analysis. (b) The excitation (broken line, emission wavelength λ = 590 nm) and emission spectra (solid line, excitation wavelength λ = 330 nm) of the CeO_2:Eu^{3+} nanocrystals. The excitation bands are attributed to Ce-O charge transfer (Ce-O CT), while the emission peaks to the Eu^{3+} ions $^5D_0$–^7F_J transitions. (For interpretation of the references to color in this figure legend, the reader is referred to the web version of this article).

The primary particle size is also evaluated by particle counting in high-angle annular dark-field scanning transmission electron microscopy (STEM-HAADF) images and their elemental composition is further validated with energy-dispersive X-ray spectroscopy (EDX). The average size of the CeO_2:Eu^{3+} determined by electron microscopy is d_{TEM} = 5.3 nm (Supplementary material, Figs. S1, S2) and is in good agreement with the d_{XRD} and d_{BET}. Importantly, the STEM-EDX elemental mapping (Supplementary material, Fig. S3) reveals the homogeneous distribution of Eu within the nanoparticles, validating that the Eu^{3+} ions are incorporated within the CeO_2 crystal matrix and do not form segregated domains. The elemental composition as determined by the EDX analysis is also in good agreement with the nominal one (5.76 at% Eu-content vs 5 at%) highlighting the efficiency of flame nanoparticle synthesis.

When Eu^{3+} ions are located inside the CeO_2 crystalline host matrix these nanocrystals become luminescent (Pratsinis et al., 2017). Fig. 1b shows the excitation (broken line, emission λ = 590 nm) and emission spectra (solid line, excitation λ = 330 nm) of the CeO_2:Eu^{3+} nanocrystals. The emission peaks of the nanocrystals due to Eu^{3+} are attributed to the $^5D_0$–^7F_J transitions (Kumar et al., 2009; Li et al., 2009), with the peak at ~590 nm from the magnetic dipole transition $^5D_0$–$^7F_1$ (Kumar et al., 2009). The excitation spectrum (Fig. 1b, broken line) has a broad band originating from the charge transfer between Ce-O (Li et al., 2009), that extends, however, to the near-UV region enabling the detection of such nanocrystals with conventional fluorescence microscopes (Spyrogianni et al., 2018), as it will be demonstrated later on.

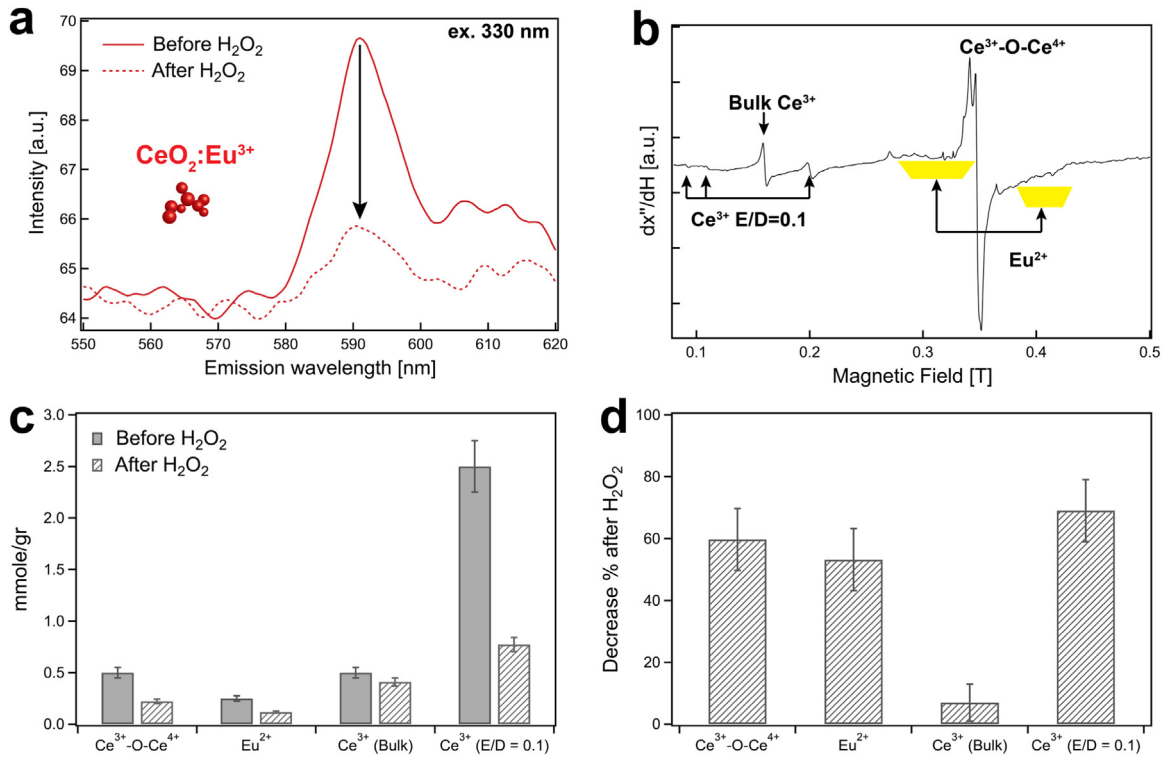

Fig. 2. (a) Emission spectra of aqueous suspensions upon excitation at λ = 330 nm before (solid lines) and after H_2O_2 (1 mM) addition (broken lines) for the $CeO_2:Eu^{3+}$ nanocrystals exhibiting the drastic luminescence quenching in the presence of H_2O_2. (b) EPR spectrum of the $CeO_2:Eu^{3+}$ nanocrystals. (c) Concentrations of different species detected by the EPR spectra before and after H_2O_2 addition. (d) Decrease (%) of each species after the addition of H_2O_2.

Fig. 2a shows the emission spectra before (solid line) and after (broken line) H_2O_2 addition in an aqueous suspension containing the $CeO_2:Eu^{3+}$ nanocrystals. The catalase-mimetic activity of these nanocrystals induces a drastic quenching of the main emission peak at λ = 590 nm upon addition of H_2O_2 (Pratsinis et al., 2017). This has been attributed to the interaction of oxygen species with the $CeO_2:Eu^{3+}$ surface that may affect the charge distribution (Cafun et al., 2013), Ce-O coordination number (Wang et al., 2015) and the oxidation state of Ce (Lee et al., 2013).

To better understand this interaction, we perform electron paramagnetic resonance (EPR) spectroscopy on these $CeO_2:Eu^{3+}$ nanocrystals. Fig. 2b shows the EPR spectrum of the $CeO_2:Eu^{3+}$ nanocrystals. Several characteristic species are detected: (i) bulk Ce^{3+} (s = 5/2), (ii) Ce^{3+}-O-Ce^{4+}, (iii) Ce^{3+} (s = 5/2) with an E/D ratio of 0.1 and (iv) several Eu^{2+} centers, presumably on the surface of the nanocrystals that have been reduced from Eu^{3+}. The Ce^{3+} species with E/D = 0.1 are observed for the first time, to the best of our knowledge, in CeO_2-based nanoparticles. From these EPR spectra it is possible to quantify the concentration of each species, and each concentration is presented in Fig. 2c before and after H_2O_2 addition. In the absence of H_2O_2 the Ce^{3+} with E/D = 0.1 have the highest concentration in these samples while the remaining species have lower concentrations (Fig. 2c). Upon the addition of H_2O_2 there are some differences observed. The concentration of most species is significantly reduced indicating its strong interaction with the $CeO_2:Eu^{3+}$ nanocrystals. To get a clearer image of the changes, the concentration decrease of each species can be calculated as a percentage (%) in Fig. 2d. From this decrease (%) it is concluded that the bulk Ce^{3+} ions are not significantly affected by the presence H_2O_2, while all other species are affected. More specifically, the largest decrease (~70%) is obtained from the newly-discovered Ce^{3+} with E/D = 0.1 that are oxidized to Ce^{4+}, while both the Eu^{2+} surface ions and the Ce^{3+}-O-Ce^{4+} ions are oxidized to Eu^{3+} and Ce^{4+}, respectively. The surface compositions and valence states of the individual $CeO_2:Eu^{3+}$ and $Y_2O_3:Tb^{3+}$ nanoparticles as well as of their hybrid nanoaggregates $CeO_2:Eu^{3+}/Y_2O_3:Tb^{3+}$ have also been measured by X-ray photoelectron spectroscopy corroborating the EPR results (Supplementary material, Fig. S4).

3.2. Robust in situ biosensing in bacterial cell cultures

The strong luminescence quenching in the presence of H_2O_2 renders the $CeO_2:Eu^{3+}$ nanocrystals powerful biosensors with limit-of-detection (LOD) down to the nM range (Pratsinis et al., 2017) outperforming most particle-based H_2O_2 biosensors in the literature, however, in this study we focus not only their sensitivity but also on their superior robustness to detect H_2O_2 levels *in situ* and in real-time during biological experiments. Therefore, and perhaps more importantly, the inorganic nature of the material enables it to be rather robust and stable in dynamic environments. To further evaluate the potential of the developed $CeO_2:Eu^{3+}$ H_2O_2 biosensors, we directly *in situ* deposit the freshly-formed $CeO_2:Eu^{3+}$ during nanoparticle synthesis by inserting a water-cooled substrate above the hot aerosol (Fig. 3a). The nanoparticles stochastically self-assemble due to thermophoresis on that substrate covering large areas homogeneously (Mädler et al., 2006). The structural stability of the self-assembled nanoparticle film can be enhanced by employing an *in situ* flame annealing step (Tricoli et al., 2008). Fig. 3b shows an SEM image of such a film deposited on a Si substrate highlighting the homogeneity and porous structure of this aerosol-deposited particle film. In fact, *in situ* flame annealing makes it possible for such porous nanoparticle films to be immersed in liquids without any particle film restructuring and/or loss (Sotiriou et al., 2013). Fig. 3c shows an SEM image of such a particle film after its immersion in aqueous solution in the presence of H_2O_2. The morphology is practically identical validating that flame annealing renders such particles films stable in liquids.

Upon mounting such a functional substrate in a custom-made flow cell made by additive manufacturing (Fig. 3d, inset), we can read-out the luminescence signal of the particle film and the sensor response can

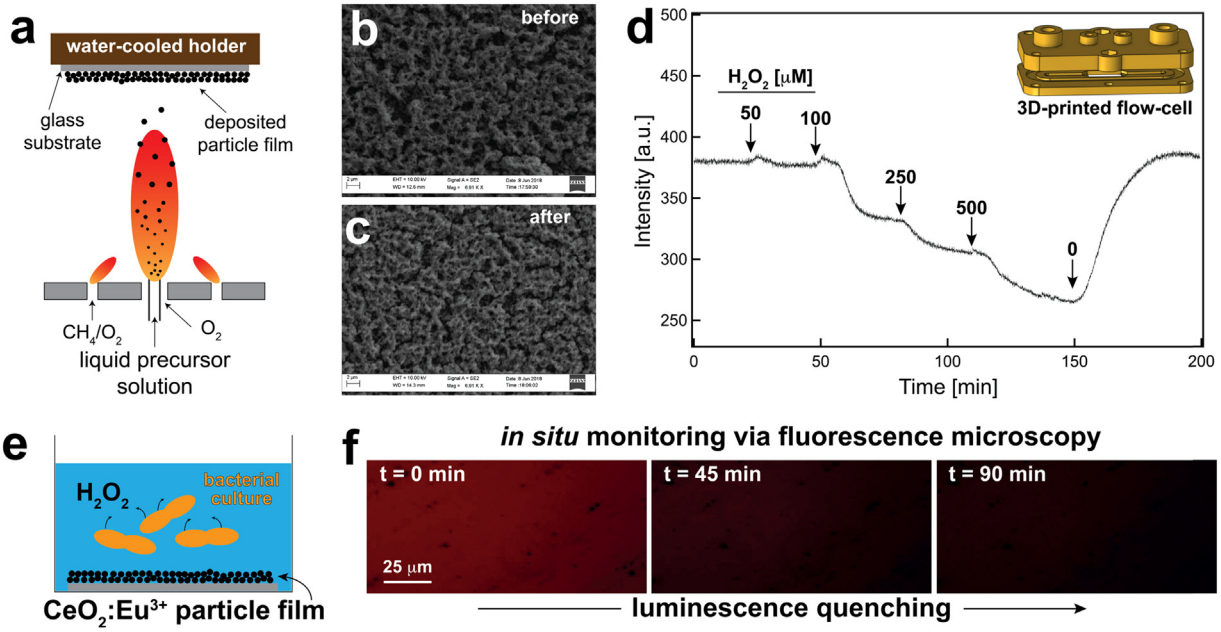

Fig. 3. (a) Schematic for the flame aerosol direct nanoparticle deposition on water-cooled substrates. (b) SEM image of deposited nanoparticle films on Si substrates before (c) and after H_2O_2 addition. (d) Luminescence signal of a CeO_2:Eu^{3+} nanoparticle film mounted on a flow-cell in various H_2O_2 concentrations (μm). (e) Schematic of the bacterial cell culture with *S. pneumoniae* (strain BHN32) in which the deposited CeO_2:Eu^{3+} nanoparticle film is located on the bottom of the well. (f) Fluorescence microscope images focusing on the CeO_2:Eu^{3+} nanoparticle films immersed in *S. pneumoniae* cell cultures for different time points (t = 0, 45 and 90 min).

be monitored in real-time under flow of various H_2O_2 concentrations. Fig. 3d shows the sensor response (luminescence intensity decrease) of such a nanoparticle film deposited on a Si substrate. The sensor response gradually changes for increasing H_2O_2 concentrations and reaches a plateau for each one only after a few minutes. Interestingly, upon flowing pure water after the sensing experiment, the sensor response returns to the initial value, indicating that the effect of the H_2O_2 species on the CeO_2:Eu^{3+} nanoparticle surface is reversible (Supplementary information, Fig. S5), but also highlighting that the developed biosensors here may be re-used several times.

To further evaluate the robustness of the developed biosensing particle films in realistic biological experiments, we utilize a rather complex biological system consisting of *S. pneumoniae* that generate H_2O_2 by converting pyruvate to acetyl phosphate and hydrogen peroxide *via* a pyruvate oxidase enzyme encoded by the spxB gene (Spellerberg et al., 1996; Syk et al., 2014). The excitation band of the CeO_2:Eu^{3+} nanocrystals extends to the near-UV (Fig. 1b, broken line) which renders it possible to utilize existing filter sets (Spyrogianni et al., 2018) in conventional fluorescence microscopes to detect their luminescence. So, upon placing the nanoparticle films (this time deposited on transparent glass coverslips) on the bottom of the microplate wells of bacterial cell cultures with *S. pneumoniae* (serotype 1 BHN32 strain (Syk et al., 2014)) and incubating them at 37 °C (Fig. 3e) in casitone and yeast solution (C+Y medium), we can monitor the luminescence intensity *in situ* with a fluorescence microscope. Fig. 3f show the characteristic red color emission from the CeO_2:Eu^{3+} nanoparticle film just at the beginning of the incubation period (t = 0 min). However, the luminescence intensity drastically decreases over time (Fig. 3g, t = 45 min) becoming almost completely diminished after t = 90 min (Fig. 3h), after which time the *S. pneumoniae* population has grown generating large amounts of H_2O_2. Therefore, the robustness of the developed biosensing nanocrystals here is validated at realistic conditions by monitoring H_2O_2 concentrations *in situ* in bacterial cell cultures.

3.3. Ratiometric hydrogen peroxide biosensing

The versatility of flame nanoparticle synthesis allows also for the production of multicomponent systems. Thus, we engineer a ratiometric H_2O_2 biosensor that allows for the rationing of the sensor signal providing a way for built-in correction and, thus, is advantageous over biosensors that utilize a single emission wavelength (Liu et al., 2011; Feng et al., 2012). That way, a non-responsive and rather stable luminescent material is employed to provide the reference signal and is combined with the CeO_2:Eu^{3+} H_2O_2-sensitive nanocrystals. For this, a double-nozzle setup is employed for the single-step production of nanomixed CeO_2:Eu^{3+}/Y_2O_3:Tb^{3+} (2.5 at% Tb^{3+}) (Sotiriou et al., 2012) hybrid nanoaggregates (Fig. 4a). The precursor molarity and flame conditions (liquid precursor feed rate, O_2 dispersion gas, please see also Experimental section) are adjusted to keep the small size of CeO_2:Eu^{3+} but yield ~30 nm Y_2O_3:Tb^{3+} nanoparticles (Sotiriou et al., 2011; Pratsinis et al., 2017). The primary particle sizes correlate with the short and long flame heights (Supplementary material, Fig. S6) of the CeO_2:Eu^{3+} and Y_2O_3:Tb^{3+} flames, respectively. Long flame heights correspond to longer residence times at high temperatures of the particles within the flame yielding, thus, larger particle sizes (Mädler et al., 2002). In the double-nozzle setup, the angle of the two nozzles is adjusted at 60° to ensure that the product nanoparticles are only mixed in the nanoscale and do not form solid solutions or mixed crystal phases that would occur in higher angles (Strobel et al., 2006). One of the main advantages of the double nozzle flame synthesis here over the single nozzle synthesis of the two individual components and their simple mechanical mixing is that the hybrid nanoaggregates are produced in a single-step, essentially halving the required nanoparticle production time and at the same time all components are present within the same nanoaggregate enabling also their utilization as particle-based sensors in fluorescence microscopes. Furthermore, pure CeO_2:Eu^{3+} nanoparticles are known to form rather large agglomerates of several hundred nanometers (Pratsinis et al., 2017) upon their dispersion in aqueous and biological buffer solutions due to their isoelectric point at pH 7.6 (Gulicovski et al., 2014). However, a further advantage of the hybrid CeO_2:Eu^{3+}/Y_2O_3:Tb^{3+} nanoaggregates here is the tuning of their

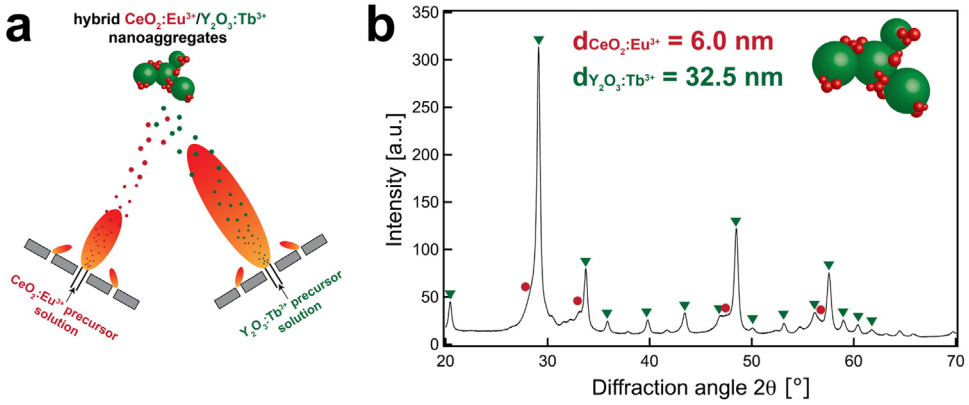

Fig. 4. (a) Schematic of double-nozzle flame reactor for the synthesis of the nano-mixed hybrid CeO_2:Eu^{3+}/Y_2O_3:Tb^{3+} nanoaggregates. The small CeO_2:Eu^{3+} nanoparticles are made in the short flame while the large Y_2O_3:Tb^{3+} nanoparticles by the long flame. The angle between the nozzle is kept at 60° to facilitate the nano-mixing of the as-prepared individual nanoparticles within the same nanoaggregates. (b) X-ray diffraction patterns of the nano-mixed CeO_2:Eu^{3+}/Y_2O_3:Tb^{3+} nanoaggregates), along with the diffraction peak positions for both the cubic Y_2O_3 (inverse triangles) and cubic CeO_2 (circles). The average crystallite sizes for each component are also displayed.

hydrodynamic diameter to significantly lower sizes (Supplementary information, Table S1 and Fig. S7).

The crystallinity of the nano-mixed CeO_2:Eu^{3+}/Y_2O_3:Tb^{3+} nanoparticles is also examined by XRD in Fig. 4b. For these nanoparticles, the cubic phase Y_2O_3 peaks (inverse triangles, ICSD: 26190) dominate the pattern, however, the CeO_2 peaks are also present (solid circles, ICSD: 61595). Rietveld refinement analysis reveals the average crystal size as well as mass fraction wt% of each crystal phase from the CeO_2:Eu^{3+} and Y_2O_3:Tb^{3+} nanoparticles that is 6 and 32.5 nm, respectively. Furthermore, the calculated mass fractions of CeO_2:Eu^{3+} and Y_2O_3:Tb^{3+} crystal phases from the XRD pattern is in excellent agreement with the nominal ones at 22 and 78 wt%, respectively (Supplementary material, Table S2). The nominal mass fractions of each individual component were tuned by adjusting the precursor molarity and liquid precursor feed rate and were selected after optimization to ensure sufficient emission intensity from the non-responsive Y_2O_3:Tb^{3+} along with the responsive CeO_2:Eu^{3+} nanoparticles (Supplementary material, Fig. S8). These results indicate that both the CeO_2:Eu^{3+} and Y_2O_3:Tb^{3+} nanoparticles are present in the nano-mixed aggregates and this is further corroborated by the specific surface area (SSA) of the CeO_2:Eu^{3+}/Y_2O_3:Tb^{3+} nanoparticles that falls in between the SSA values of the individual samples (Supplementary material, Table S2).

The morphology and composition of the CeO_2:Eu^{3+}/Y_2O_3:Tb^{3+} nanoaggregates is further studied by STEM-HAADF along with EDX. Fig. 5a shows an STEM-HAADF image of the CeO_2:Eu^{3+}/Y_2O_3:Tb^{3+} nanoaggregates in which both large and small nanoparticles can be detected. Fig. 5a also shows the elemental mapping of this image tracking the presence of Y (green signal), Ce (red signal) and both Y and Ce (composite image), validating that both small CeO_2:Eu^{3+} and large Y_2O_3:Tb^{3+} nanoparticles are present in the CeO_2:Eu^{3+}/Y_2O_3:Tb^{3+} nanoaggregates and that they are segregated (for EDX spectrum see Supplementary material, Fig. S9). These nanoaggregates exhibit a bimodal particle size distribution (Fig. 5b) with a mode around 5 nm and another one around 30 nm in excellent agreement with the particle size distributions of the individual samples (Supplementary material, Figs. S2 and S10,S11), additionally verifying that both the small CeO_2:Eu^{3+} and large Y_2O_3:Tb^{3+} nanoparticles are present in the nanoaggregates.

Both CeO_2:Eu^{3+} and Y_2O_3:Tb^{3+} are luminescent upon the same UV excitation wavelength λ = 330 nm. The main emission wavelength due to the Tb^{3+} ions in Y_2O_3 crystal host matrix is at 545 nm ($^5D_4$–$^7F_5$ transition) (Mukherjee et al., 2008) distinctly different that the one due to the Eu^{3+} ions in CeO_2 crystal host matrix around 590 nm ($^5D_0$–$^7F_1$ transition) (Kumar et al., 2009; Li et al., 2009). Fig. 6a indeed shows the emission spectra of aqueous suspension from the CeO_2:Eu^{3+}/Y_2O_3:Tb^{3+} nanoaggregates upon excitation at 330 nm, before (solid lines) and after 1 mM H_2O_2 addition (broken lines). The luminescence intensity of the Y_2O_3:Tb^{3+} is not affected by the addition of H_2O_2, however, the one from CeO_2:Eu^{3+} is significantly quenched. Thus,

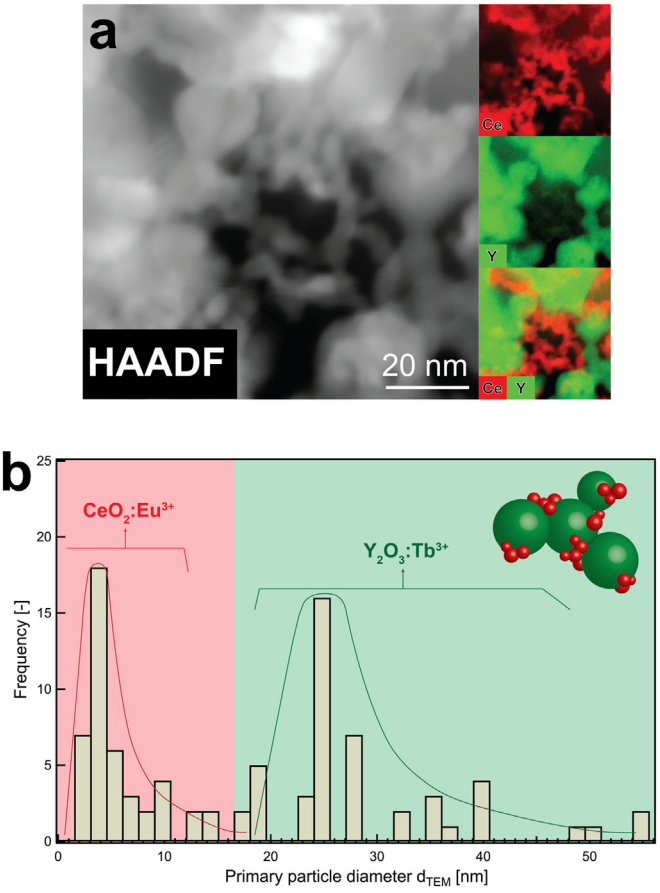

Fig. 5. (a) High-angle annular dark-field scanning transmission electron microscopy (STEM-HAADF) of the nano-mixed CeO_2:Eu^{3+}/Y_2O_3:Tb^{3+} and its elemental mapping for Ce in red, for Y in green, Ce and Y in a composite image verifying the presence of small CeO_2:Eu^{3+} and large Y_2O_3:Tb^{3+} nanoparticles in these nanoaggregates. (b) The measured particle size d_{TEM} distribution for n = 92. There are both large and small crystalline nanoparticles observed with a bimodal particle size distribution. (For interpretation of the references to color in this figure legend, the reader is referred to the web version of this article).

monitoring the ratio of the two emission intensities at wavelengths λ = 590 and 545 nm (I_{590}/I_{545}) allows for ratiometric H_2O_2 detection.

The potential of such a ratiometric H_2O_2 biosensor is further examined by monitoring the sensor response R as a function of a wide range of H_2O_2 concentration in C + Y medium. Fig. 6b shows this sensor response curve (yellow circles) calculated ratiometrically. Sensor response S_R is calculated by $S_R = 1-(R_S/R_0)$, where R_S is the ratiometric (I_{590}/I_{545}) signal of samples with various H_2O_2 concentrations, and R_0 is

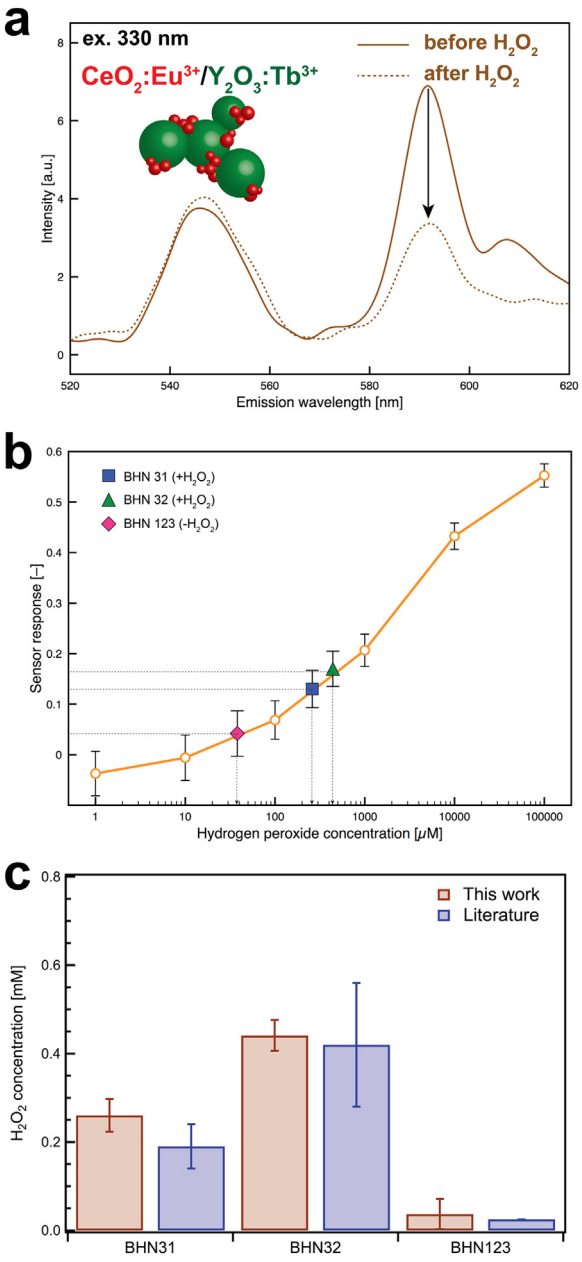

Fig. 6. (a) Emission spectra of aqueous suspensions upon excitation at $\lambda = 330$ nm before (solid lines) and after H_2O_2 (1 mM) addition (broken lines) for nano-mixed CeO_2:Eu^{3+}/Y_2O_3:Tb^{3+} nanoaggregates. The CeO_2:Eu^{3+}/Y_2O_3:Tb^{3+} nanoaggregates exhibit the emission from both components attributed to Y_2O_3:Tb^{3+} ($\lambda = 545$ nm) and CeO_2:Eu^{3+} ($\lambda = 590$ nm) enabling the ratiometric determination of H_2O_2 concentrations. (b) H_2O_2 sensor response determined ratiometrically from the CeO_2:Eu^{3+}/Y_2O_3:Tb^{3+} nanoaggregates in the presence of a broad range of H_2O_2 concentrations in C+Y cell culture medium (n = 3). The sensor signal from bacterial cultures with three *S. pneumoniae* strains, two strains that generate high amounts of H_2O_2, BHN31 (blue square) and BHN32 (green triangle) as well as one genetically-modified strain that does not generate H_2O_2, BHN123 (red diamond) are also shown. (c) The generated H_2O_2 concentrations from the three *S. pneumoniae* strains as determined from this study with the ratiometric CeO_2:Eu^{3+}/Y_2O_3:Tb^{3+} nanoaggregates (red bars, n = 3) and reported in the literature (Syk et al., 2014) by commercial peroxidase-based assays (blue bars). For strain BHN123 the H_2O_2 concentration reported in the literature was < 0.025 mM that is the limit of detection of the used assay. (For interpretation of the references to color in this figure legend, the reader is referred to the web version of this article).

the ratiometric signal of pure H_2O. The H_2O_2 response concentration range spans several orders of magnitude, rendering this H_2O_2 biosensor suitable for studies where H_2O_2 concentrations are unknown. It should be noted that the CeO_2:Eu^{3+} nanoparticles that are responsive to H_2O_2 exhibit high selectivity over a wide range of other analytes such as ions (K^+, Na^+, PO_4^{3-}, Cl^-, Fe^{3+}, NO_3^-), proteins (serum) and negatively charged and neutral amino acids, but there is some interference from antioxidants (*e.g.* uric acid, ascorbic acid) and positively charged amino acids (Pratsinis et al., 2017). Nonetheless, the response curve in Fig. 6b indicates that our biosensor is functional in biological buffers over a rather broad (> 4 orders of magnitude) range. Furthermore, it should be noted that the developed nanoaggregates here exhibit high optical and chemical stability due to their inorganic nature (Supplementary material, Fig. S12) in agreement with the literature for the single CeO_2:Eu^{3+} nanoparticles (Pratsinis et al., 2017).

Furthermore, we test two pneumococcal serotype 1 clinical isolates that generate high amounts of H_2O_2 (BHN31 and BHN32) as well as one genetically-modified strain that lacks the spxB gene (ΔspxB mutant strain, BHN123) and, thus, does not generate H_2O_2 (Syk et al., 2014). After incubation of the strains in C+Y medium to reach mid-log phase (OD_{620}: 0.3–0.4) we neutralize the growth by adding penicillin and measure the produced H_2O_2 concentrations using our ratiometric biosensors. Fig. 6b also shows the sensor response of the BHN31 (blue square), BHN32 (green triangle) and BHN123 (red diamond) that is fitted onto the sensor response curve by logarithmic interpolation between the two adjacent data points. The resulting H_2O_2 concentrations of the three individual strains is also plotted in Fig. 6c (red bars) and directly compared with the values reported in the literature acquired by conventional peroxidase-based assays (blue bars) (Syk et al., 2014). The H_2O_2 determination from our biosensors is in excellent agreement with the reported values in the literature, with lower standard deviation, further highlighting the functionality of the developed all inorganic nanoparticle-based H_2O_2 biosensors here and verifies their suitability as a robust H_2O_2 sensing tool.

4. Conclusions

We present here the rational design and flame spray synthesis of CeO_2:Eu^{3+} nanocrystals and evaluate their performance as a luminescent robust H_2O_2 biosensor. The small size of the developed CeO_2:Eu^{3+} nanocrystals facilitates their interactions with H_2O_2 in solution drastically affecting their electronic and luminescent properties. Upon the direct nanoparticle aerosol deposition on Si and glass substrates during flame synthesis, functional nanoparticle films can be produced that may be employed in bacterial cell cultures to detect *in situ* in real-time H_2O_2 concentrations with a fluorescence microscope. Furthermore, double-nozzle flame synthesis is employed to develop nanoaggregates that consist of H_2O_2-sensitive CeO_2:Eu^{3+} nanoparticles, and non-responsive larger Y_2O_3:Tb^{3+} nanoparticles. Even though the luminescence intensity of the CeO_2:Eu^{3+} nanocrystals is drastically quenched in the presence of H_2O_2, the luminescence of the Y_2O_3:Tb^{3+} nanoparticles is unaffected rendering these hybrid nanoaggregates robust optical-based ratiometric H_2O_2 biosensors. Both components are luminescent upon the same UV excitation wavelength simultaneously, avoiding the need to perform two separate measurements and correlate them afterwards in a second step. Furthermore, the developed biosensor here consists of purely inorganic materials, and thus, it is highly robust with long shelf-life in ambient conditions and it is further suitable for autoclave processes without the risk of degradation. The biosensor response is examined here by monitoring the luminescence intensity of the two emission wavelengths corresponding to the CeO_2:Eu^{3+} and Y_2O_3:Tb^{3+} nanoparticles, respectively, in a broad range of H_2O_2 concentrations in biological-relevant solutions. In fact, the biosensor performance is explored beyond simple biosensing in buffer solutions towards measurements under realistic conditions in complex bacterial cell cultures *in vitro* by detecting the generated H_2O_2 concentration from clinically-

relevant *S. pneumoniae* strains. The luminescent CeO_2:Eu^{3+} developed here could set the basis for facile and robust H_2O_2 detection using *in vitro* assays.

Supplementary material

Additional data regarding the characterization and biosensing performance of the developed luminescent nanoparticles.

CRediT authorship contribution statement

Dorian F. Henning: Data curation, Formal analysis, Methodology, Visualization, Writing - review & editing. **Padryk Merkl:** Data curation, Methodology, Formal analysis, Visualization, Writing - review & editing. **Changhun Yun:** Data curation, Formal analysis, Writing - review & editing. **Federico Iovino:** Data curation, Formal analysis, Visualization, Writing - review & editing. **Ling Xie:** Data curation, Formal analysis, Writing - review & editing. **Eleftherios Mouzourakis:** Data curation, Formal analysis, Writing - review & editing. **Constantinos Moularas:** Data curation, Formal analysis, Writing - review & editing. **Yiannis Deligiannakis:** Resources, Formal analysis, Writing - review & editing. **Birgitta Henriques-Normark:** Resources, Writing - review & editing. **Klaus Leifer:** Resources, Writing - review & editing. **Georgios A. Sotiriou:** Conceptualization, Supervision, Formal analysis, Funding acquisition, Methodology, Resources, Visualization, Writing - original draft, Writing - review & editing.

Acknowledgements

This project has received funding from the European Research Council (ERC) under the European Union's Horizon 2020 research and innovation programme (ERC Grant agreement n° 758705). Funding from the Karolinska Institutet Board of Research, the Swedish Research Council (2016-03471), the Jeansson Foundations (JS2016-0029) and the Åke Wiberg Foundation (M16-0098) is kindly acknowledged. D. Henning carried out part of this research as an exchange MSc student from ETH Zurich, Switzerland.

Declaration of interests

None.

Author contributions

G.A.S.: Conceptualization, Supervision, Formal analysis, Funding acquisition, Methodology, Resources, Visualization, Writing - original draft, Writing - review & editing. D.F.H.: Data curation, Formal analysis, Methodology, Visualization, Writing - review & editing. C.Y.: Data curation, Formal analysis, Writing - review & editing. P.M.: Data curation, Methodology, Formal analysis, Visualization, Writing - review & editing. F.I.: Data curation, Formal analysis, Visualization, Writing - review & editing. B.H.N.: Resources, Writing - review & editing. L.X.: Data curation, Formal analysis, Writing - review & editing. K.L.: Resources, Writing - review & editing. E.M.: Data curation, Formal analysis, Writing - review & editing. C.M.: Data curation, Formal analysis, Writing - review & editing. Y.D.: Resources, Formal analysis, Writing - review & editing.

Appendix A. Supporting information

Supplementary data associated with this article can be found in the online version at doi:10.1016/j.bios.2019.03.012.

References

Andisi, V.F., Hinojosa, C.A., de Jong, A., Kuipers, O.P., Orihuela, C.J., Bijlsma, J.J.E., 2012. Infect. Immun. 80, 1037–1049.
Büchel, R., Strobel, R., Krumeich, F., Baiker, A., Pratsinis, S.E., 2009. J. Catal. 261, 201–207.
Cafun, J.D., Kvashnina, K.O., Casals, E., Puntes, V.F., Glatzel, P., 2013. ACS Nano 7, 10726–10732.
Duee, N., Ambard, C., Pereira, F., Portehault, D., Viana, B., Valle, K., Autissier, D., Sanchez, C., 2015. Chem. Mater. 27, 5198–5205.
Feng, Y., Cheng, J.H., Zhou, L., Zhou, X.G., Xiang, H.F., 2012. Analyst 137, 4885–4901.
Grossmann, H.K., Grieb, T., Meierhofer, F., Hodapp, M.J., Noriler, D., Grohn, A., Meier, H.F., Fritsching, U., Wegner, K., Madler, L., 2015. J. Nanopart. Res. 17, 174.
Gulicovski, J.J., Bracko, I., Milonjic, S.K., 2014. Mater. Chem. Phys. 148, 868–873.
Gupta, A., Das, S., Neal, C.J., Seal, S., 2016. J. Mater. Chem. B 4, 3195–3202.
Gupta, A., Rawal, T.B., Neal, C.J., Das, S., Rahman, T.S., Seal, S., 2017. 2D Mater. 4, 025077.
Halliwell, B., Clement, M.V., Long, L.H., 2000. FEBS Lett. 486, 10–13.
Henriques-Normark, B., Tuomanen, E.I., 2013. Cold Spring Harb. Perspect. Med. 3, a010215.
Iovino, F., Seinen, J., Henriques-Normark, B., van Diji, J.M., 2016. Trends Microbiol. 24, 307–315.
Kumar, A., Babu, S., Karakoti, A.S., Schulte, A., Seal, S., 2009. Langmuir 25, 10998–11007.
Lee, S.S., Song, W.S., Cho, M.J., Puppala, H.L., Nguyen, P., Zhu, H.G., Segatori, L., Colvin, V.L., 2013. ACS Nano 7, 9693–9703.
Li, L., Yang, H.K., Moon, B.K., Fu, Z.L., Guo, C.F., Jeong, J.H., Yi, S.S., Jang, K., Lee, H.S., 2009. J. Phys. Chem. C 113, 610–617.
Li, Y.Y., He, X., Yin, J.J., Ma, Y.H., Zhang, P., Li, J.Y., Ding, Y.Y., Zhang, J., Zhao, Y.L., Chai, Z.F., Zhang, Z.Y., 2015. Angew. Chem. -Int. Ed. 54, 1832–1835.
Liu, B.W., Sun, Z.Y., Huang, P.J.J., Liu, J.W., 2015. J. Am. Chem. Soc. 137, 1290–1295.
Liu, J.L., Liu, Y., Liu, Q., Li, C.Y., Sun, L.N., Li, F.Y., 2011. J. Am. Chem. Soc. 133, 15276–15279.
Lv, C.J., Di, W.H., Liu, Z.H., Zheng, K.Z., Qin, W.P., 2014. Analyst 139, 4547–4555.
Mädler, L., Stark, W.J., Pratsinis, S.E., 2002. J. Mater. Res. 17, 1356–1362.
Mädler, L., Roessler, A., Pratsinis, S.E., Sahm, T., Gurlo, A., Barsan, N., Weimar, U., 2006. Sens. Actuator B-Chem. 114, 283–295.
Mukherjee, S., Sudarsan, V., Vatsa, R.K., Godbole, S.V., Kadam, R.M., Bhatta, U.M., Tyagi, A.K., 2008. Nanotechnology 19, 325704.
Pratsinis, A., Kelesidis, G.A., Zuercher, S., Krumeich, F., Bolisetty, S., Mezzenga, R., Leroux, J.C., Sotiriou, G.A., 2017. ACS Nano 11, 12210–12218.
Pratsinis, S.E., 2010. AIChE J. 56, 3028–3035.
de la Rica, R., Stevens, M.M., 2012. Nat. Nanotechnol. 7, 821–824.
Sotiriou, G.A., Schneider, M., Pratsinis, S.E., 2011. J. Phys. Chem. C 115, 1084–1089.
Sotiriou, G.A., Schneider, M., Pratsinis, S.E., 2012. J. Phys. Chem. C 116, 4493–4499.
Sotiriou, G.A., Blattmann, C.O., Pratsinis, S.E., 2013. Adv. Funct. Mater. 23, 34–41.
Spellerberg, B., Cundell, D.R., Sandros, J., Pearce, B.J., Idänpään-Heikkilä, I., Rosenow, C., Masure, H.R., 1996. Mol. Microbiol. 19, 803–813.
Spyrogianni, A., Tiefenboeck, P., Starsich, F.H.L., Keevend, K., Krumeich, F., Herrmann, I.K., Leroux, J.C., Sotiriou, G.A., 2018. AIChE J. 64, 2947–2957.
Strobel, R., Madler, L., Piacentini, M., Maciejewski, M., Baiker, A., Pratsinis, S.E., 2006. Chem. Mater. 18, 2532–2537.
Syk, A., Norman, M., Fernebro, J., Gallotta, M., Farmand, S., Sandgren, A., Normark, S., Henriques-Normark, B., 2014. J. Infect. Dis. 210, 4–13.
Tricoli, A., Graf, M., Mayer, F., Kuühne, S., Hierlemann, A., Pratsinis, S.E., 2008. Adv. Mater. 20, 3005–3010.
Walkey, C., Das, S., Seal, S., Erlichman, J., Heckman, K., Ghibelli, L., Traversa, E., McGinnis, J.F., Self, W.T., 2015. Environ. -Sci. Nano 2, 33–53.
Wang, Y.J., Dong, H., Lyu, G.M., Zhang, H.Y., Ke, J., Kang, L.Q., Teng, J.L., Sun, L.D., Si, R., Zhang, J., Liu, Y.J., Zhang, Y.W., Huang, Y.H., Yan, C.H., 2015. Nanoscale 7, 13981–13990.
Wei, H., Wang, E.K., 2013. Chem. Soc. Rev. 42, 6060–6093.
Yang, L.M., Li, N., Pan, W., Yu, Z.Z., Tang, B., 2015. Anal. Chem. 87, 3678–3684.
Yang, L.M., Ren, Y.F., Pan, W., Yu, Z.Z., Tong, L.L., Li, N., Tang, B., 2016. Anal. Chem. 88, 11886–11891.
Yuan, J.P., Guo, W.W., Yin, J.Y., Wang, E.K., 2009. Talanta 77, 1858–1863.
Zeng, H.H., Qiu, W.B., Zhang, L., Liang, R.P., Qiu, J.D., 2016. Anal. Chem. 88, 6342–6348.
Zeng, H.H., Zhang, L., Rong, L.Q., Liang, R.P., Qiu, J.D., 2017. Biosens. Bioelectron. 89, 721–727.
Zheng, H., Su, R.X., Gao, Z., Qi, W., Huang, R.L., Wang, L.B., He, Z.M., 2014. Anal. Methods 6, 6352–6357.